ACS APPLIED MATERIALS & INTERFACES

Research Article

www.acsami.org

Tremendous Effect of the Morphology of Birnessite-Type Manganese Oxide Nanostructures on Catalytic Activity

Jingtao Hou, Yuanzhi Li,* Mingyang Mao, Lu Ren, and Xiujian Zhao

State Key Laboratory of Silicate Materials for Architectures, Wuhan University of Technology, 122 Luoshi Road, Wuhan 430070, China

Supporting Information

ABSTRACT: The octahedral layered birnessite-type manganese oxide (OL-1) with the morphologies of nanoflowers, nanowires, and nanosheets were prepared and characterized with X-ray diffraction (XRD), scanning electron microscopy (SEM), transmission electron microscopy (TEM), thermogravimetric/differential scanning calorimetry (TG/DSC), Brunnauer–Emmett–Teller (BET), inductively coupled plasma (ICP), and X-ray photoelectron spectroscopy (XPS). The OL-1 nanoflowers possess the highest concentration of oxygen vacancies or Mn^{3+}, followed by the OL-1 nanowires and nanosheets. The result of catalytic tests shows that the OL-1 nanoflowers exhibit a tremendous enhancement in the catalytic activity for benzene oxidation as compared to the OL-1 nanowires and nanosheets. Compared to the OL-1 nanosheets, the OL-1 nanoflowers demonstrate an enormous decrease (ΔT_{50} = 274 °C; ΔT_{90} > 248 °C) in reaction temperatures T_{50} and T_{90} (corresponding to 50 and 90% benzene conversion, respectively) for benzene oxidation. The origin of the tremendous effect of morphology on the catalytic activity for the nanostructured OL-1 catalysts is experimentally and theoretically studied via CO temperature-programmed reduction (CO-TPR) and density functional theory (DFT) calculation. The tremendous catalytic enhancement of the OL-1 nanoflowers compared to the OL-1 nanowires and nanosheets is attributed to their highest surface area as well as their highest lattice oxygen reactivity due to their higher concentration of oxygen vacancies or Mn^{3+}, thus tremendously improving the catalytic activity for the benzene oxidation.

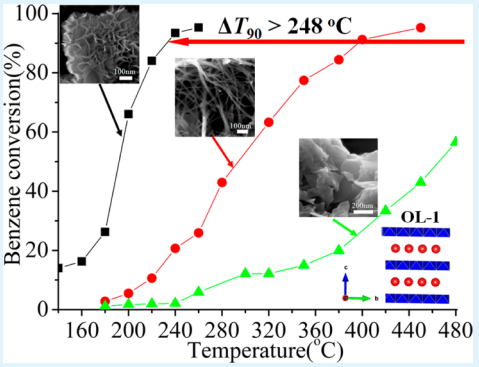

KEYWORDS: *catalytic, manganese oxide, morphology effect, oxygen vacancy*

1. INTRODUCTION

Volatile organic compounds (VOCs) as major air pollutants are not only hazardous to human health but also harmful to the environment. It is highly desirable to develope technology for purifying VOCs. Among various VOCs, the carcinogenic and recalcitrant benzene has been regarded as a priority hazardous pullutant for which efficient purification technology is needed.[1−9] Catalytic oxidation is one of the most efficient technologies for complete oxidation of VOCs to CO_2 and H_2O.[3−9] Expensive supported noble metals (e. g., Pt, Pd, Rh, and Au) are conventionally used as the most efficient catalysts in the catalytic oxidation of VOCs.[5−9] It is challenging and significant to find economical catalysts alternative to noble metal catalysts. Octahedral layered birnessite (OL-1) with formula of $A_xMnO_{2-y}\cdot zH_2O$ (where A is H^+ or metal cation), which is inexpensive and environmentally benign, is a type of manganese oxide having edge-shared MnO_6 octahedral forming a two-dimensional (2D) layer structure with exchangeable cations (e. g., K^+, Na^+) and water molecules located at the interlayer space (0.70 nm).[10−15] Due to its distinctive chemical and physical properties, OL-1 has been extensively investigated for diverse applications such as heavy metal ion adsorption,[12,13] cathodes for rechargeable lithium batteries,[14,15] electrochemical capacitors,[16,17] magnetic materials,[18,19] water oxidation,[20,21] electrocatalytic oxygen reduction,[22] and the catalytic oxidation of volatile organic compounds (VOCs),[23−27] CO,[28] soot combustion,[29] phenol,[30] and benzyl alcohol,[31] etc. Among the applications, the catalytic application has received scientific interests as OL-1 exhibits an unique structural characteristics such as porous structure, mixed valence (3+, and 4+) of Mn, easy release of lattice oxygen, etc.,[10] which result in its high activity for catalytic oxidation. It has been reported that the catalytic activity of nanostructured OL-1 is dependent on its morphology, particle size, surface area, and surface reducibility.[23,24] It is scientifically and technologically significant to develop a strategy of improving the catalytic activity of OL-1 in order to make OL-1 an economically exciting alternative to noble metal catalysts. However, only very few efforts have been made in improving the catalytic activity of OL-1 such as by controlling the morphology of nanostructured OL-1[23,24] and Co ion doping of OL-1.[28] Herein, we develop a novel and facile approach of hydrothermal redox reaction to prepare OL-1 nanoflowers. Their catalytic activity for benzene oxidation is compared with the catalysts of OL-1 nanowires and nanosheets.

Received: May 7, 2014
Accepted: August 20, 2014
Published: August 20, 2014

   dx.doi.org/10.1021/am5027743 | ACS Appl. Mater. Interfaces 2014, 6, 14981−14987

For the first time, we demonstrate a giant effect of morphology on the catalytic activity of nanostructured OL-1. The OL-1 nanoflowers exhibit a tremendous enhancement in the catalytic activity as compared to the OL-1 nanowires and nanosheets. We reveal by combining both theoretical and experimental evidence that the tremendous catalytic enhancement of OL-1 nanoflowers is attributed to their highest lattice oxygen reactivity due to their higher oxygen vacancy or Mn^{3+} concentration.

2. EXPERIMENTAL SECTION

Preparation. OL-1 nanoflower sample was prepared by a facile method of hydrothermal reaction between $Mn(NO_3)_2$ and $KMnO_4$. The detailed procedure is as follows: 3.5790 g of $Mn(NO_3)_2$(50 wt %) was dissolved in 40 mL of distilled water in a beaker; 3.1608 g of $KMnO_4$ was added into the $Mn(NO_3)_2$ aqueous solution under vigorous magnetic stirring until it was dissolved. Then, the solution was transferred to a 100 mL Teflon bottle, which was sealed tightly in a stainless-steel autoclave. The autoclave was heated to 50 °C in an electrical oven and kept at the temperature for 48 h. After the autoclave cooled to ambient temperature, the precipitate was thoroughly washed with distilled water and dried under an infrared lamp.

The OL-1 nanowire sample was prepared according to the similar procedure reported by Liang et al.:[28] 0.11 g of $MnSO_4{\cdot}H_2O$ and 0.60 g of $KMnO_4$ were added into 32 mL of distilled water under magnetic stirring until they were dissolved. Then, the solution was transferred to a 100 mL Teflon bottle, which was sealed tightly in a stainless-steel autoclave. The autoclave was placed in an electric oven, heated to 240 °C and kept at the temperature for 24 h. After the autoclave had cooled to room temperature, the precipitate was thoroughly washed with distilled water and dried at 90 °C for 12 h.

The OL-1 nanosheet sample was prepared according to the similar procedure reported by Duan et al.[17] 0.948 g of $KMnO_4$ was dissolved into 15 mL of distilled water. The solution was transferred to a 100 mL Teflon bottle, which was sealed tightly in a stainless-steel autoclave. The autoclave was placed in an electrical oven, heated to 240 °C and kept at the temperature for 24 h. After the autoclave had cooled to room temperature, the precipitate was thoroughly washed with distilled water and dried at 90 °C for 12 h.

Characterization. X-ray diffraction (XRD) patterns were observed on a Rigaku Dmax X-ray diffractometer using Cu Kα radiation. Scanning electron microscopy (SEM) images were obtained by using a Hitachi S-4800 scanning electron microscope. Transmission electron microscopy (TEM) images were obtained by using a JEM-100CX electron microscope. The surface area of the OL-1 samples was measured on ASAP2020 using N_2 adsorption at −196 °C. The chemical compositions of the OL-1 samples were measured by inductively coupled plasma/optical emission spectroscopy (ICP-OES, PerkinElmer Optima 4300DV). Thermogravimetric/differential scanning calorimetric (TG/DSC) analysis was performed on a NETZSCH STA 449F3 thermal analyzer in air at a heating rate of 10 °C min^{-1}. The OL-1 samples were analyzed by a VG Multilab 2000 X-ray photoelectron spectrometer (XPS) using Mg Kα radiation. The XPS spectra of the OL-1 samples were calibrated by referencing the binding energy to adventitious carbon (C 1s 284.6 eV) and were deconvoluted using special software. CO temperature-programmed reduction (CO-TPR) and O_2 temperature-programmed oxidation (O_2-TPO) were conducted on a TP-5080 multifunctional adsorption apparatus equipped with a TCD detector. The details are described in our previous works.[3,4]

DFT Calculation Method. Density functional theory (DFT) calculations[32−37] were used to study birnessite-type MnO_2 (OL-1). The details of DFT calculation methodology are described in our previous works.[3,4,32−37] Our calculated lattice parameters of bulk OL-1 with monoclinic birnessite structure are a = 5.149, b = 2.843, c = 7.176 Å, $\alpha = \gamma = 90°$, β = 100.76° (JCPDS 80-1098). To ensure the convergence of the calculations, we repeated all the calculations with a larger super cell ($K_8Mn_{32}O_{64}$) of 104 atoms (2 × 4 × 2), which is similar to the literature reported by Kwon et al.[38]

Catalytic Activity. The catalytic activity measurements for the catalytic oxidation of benzene were carried out at atmospheric pressure in a continuous flow fixed-bed quartz tubular reactor on a WFS-2015 online gas-phase reaction apparatus. The details of catalytic activity measurement and product analysis using gas chromatograph are described in our previous works.[3,4]

3. RESULTS AND DISCUSSION

3.1. Characterization. The sample of OL-1 nanoflowers (denoted as OL-1 NF) was prepared by a novel and facile approach of hydrothermal redox reaction between $Mn(NO_3)_2$ and $KMnO_4$ at 50 °C. The samples of OL-1 nanowires and nanosheets (denoted as OL-1 NW and OL-1 NS) were prepared according to the similar procedures reported by Liang et al.[28] and Duan et al.[17](Experimental Section), respectively. Figure 1 shows the XRD patterns of the as-prepared OL-1

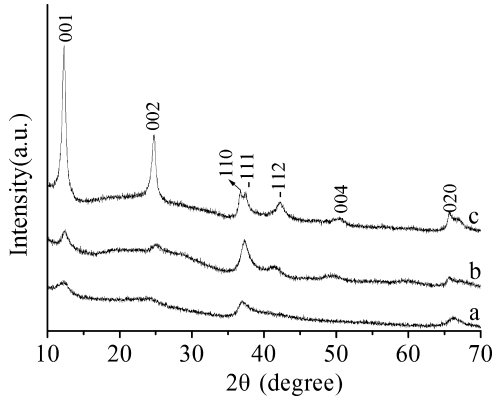

Figure 1. XRD patterns of (a) OL-1 NF, (b) OL-1 NW, and (c) OL-1 NS.

samples. The XRD analysis reveals that all the as-synthesized OL-1 samples have a pure birnessite structure (JCPDS 80-1098, $K_{0.46}Mn_2O_4{\cdot}1.4H_2O$). Compared to OL-1 NS, both OL-1 NF and OL-1 NW exhibit broader diffraction peaks, indicating their smaller crystal sizes. The average crystal size of OL-1 NF, OL-1 NW, and OL-1 NS, determined by using the Scherrer formula ($L = 0.89\lambda/\beta \cos\theta$) at 2θ = 12.3° (corresponding to {001} plane), is 5.9, 9.0, and 15.3 nm, respectively.

Figure 2 shows the SEM and TEM images of the OL-1 NF sample. The OL-1 NF sample is characterized by the morphology of nanoflowers (Figure 2a and c), each of which comprises a number of nanoflakes with sizes of ∼500 nm (Figure 2b). The thickness of two hundred nanoflakes in the SEM image of OL-1 nanoflowers was measured. The thickness size distribution of the nanoflakes in OL-1 nanoflowers reveals that their dominant size is 4−6 nm (Supporting Information Figure S1). The arithmetic average thickness of the nanoflakes is calculated to be 5.9 nm, which is in agreement to the average crystal size (corresponding to {001} plane) determined by XRD. High-resolution TEM (HRTEM) images show {100} facet with lattice spacing of 0.50 nm on the top of a nanoflake of OL-1 NF and {001} facet with lattice spacings of 0.70 nm on the side of another nanoflake. Scanning electron microscopy (SEM) and transmission electron microscopy (TEM) images (Figure S2 and S3, Supporting Information) show that OL-1 NW is characterized by the morphology of nanowires with lengths of ∼3 μm and diameters of ∼5 nm, while OL-1 NS is

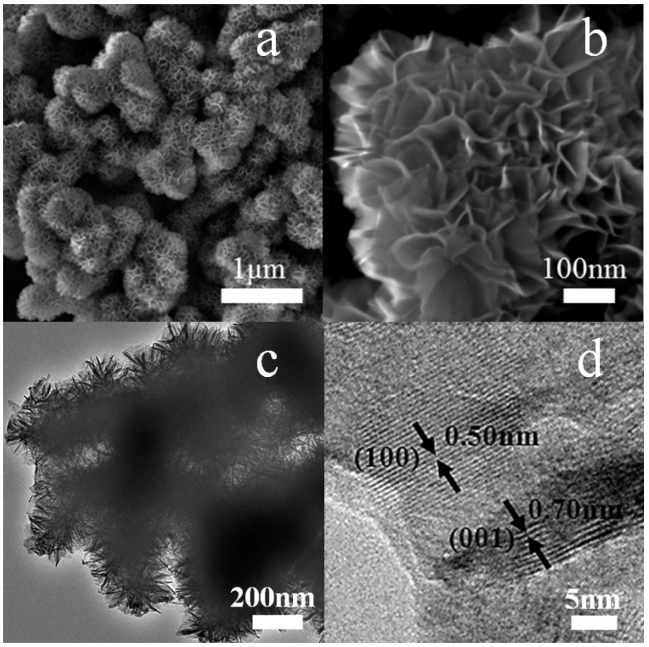

Figure 2. SEM (a, b) and TEM (c, d) images of OL-1 NF.

characterized by the morphology of nanosheets with thicknesses of ~20 nm and sizes up to micrometers. HRTEM images indicate that both OL-1 NW and OL-1 NS have {100} facet with lattice spacing of 0.50 nm (Supporting Information Figure S3b and d).

The N_2 adsorption/desorption reveals that the Brunauer–Emmett–Teller (BET) surface area of OL-1 nanoflowers, nanowires, and nanosheets is 162.6, 98.0, and 19.0 $m^2\ g^{-1}$, respectively (Table 1, Supporting Information Figure S4). The micropore surface area of the OL-1 samples is obtained by using the t-plot method.[39] As shown in Table 1, the t-plot method micropore surface area of OL-1 nanflowers, nanowires, and nanosheets is 45.4, 21.2, and 3.4 $m^2\ g^{-1}$, respectively. The bulk composition of the OL-1 samples was analyzed by the inductively coupled plasma-optical emission spectroscopy (ICP-OES) analyses. The K/Mn atomic ratio of OL-1 nanflowers, nanowires, and nanosheets is 0.10, 0.25, and 0.33, respectively (Table 1).

Thermogravimetric/differential scanning calorimetry (TG/DSC) analysis of the OL-1 nanoflower sample shows a large endothermic peak around 75 °C and shoulder peak around 125 °C accompanied by a weight loss of 13.70% below 280 °C, which are attributed to physisorbed and interlayer water in birnessite nanostructure (Supporting Information Figure S5).[18,24,40] Above 300 °C, the oxygen release is evolved due to the partial reduction of Mn^{4+} to Mn^{3+}. The exothermic peak around 491 °C on DSC curve is related to the phase transformation from the layered structure of OL-1 to the α-MnO_2 phase,[18,24] and the weight increase of 0.34% on the corresponding TG curve indicates that the released oxygen is partly compensated due to the oxidation of Mn^{3+} to Mn^{4+} during this phase transformation.[18,24] The two endothermic peaks accompanied by weight losses of 1.63% and 2.06% around 864 and 949 °C are related to the structure transformation from MnO_2 to Mn_2O_3 and from Mn_2O_3 to Mn_3O_4, respectively.[18]

The oxidation state of Mn in the OL-1 samples with different morphologies are qualitatively analyzed by studying the Mn 2p spectra.[41−45] The Mn 2p spectra of all OL-1 samples are decomposed into four peaks (Figure 3A). Two peaks around

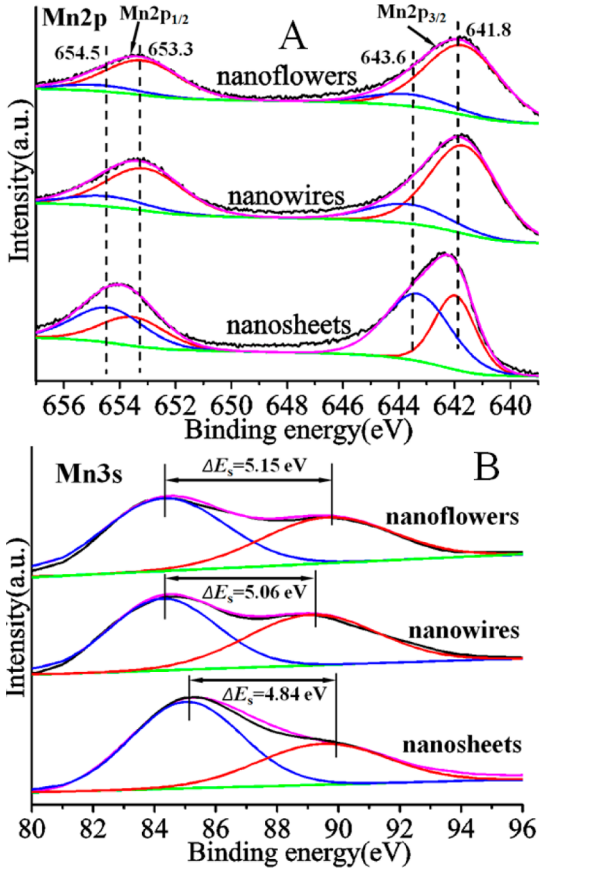

Figure 3. Mn 2p (A) and Mn 3s (B) XPS spectra of the OL-1 samples.

~641.8 and ~653.3 eV are assigned to Mn $2p_{3/2}$ and Mn $2p_{1/2}$ of Mn^{3+} species, respectively, while two peaks around ~643.6 and ~654.5 eV are assigned to those of Mn^{4+} species.[42−44] No Mn^{2+} species are detected by XPS. As shown in Table 1, OL-1 nanoflowers possess the highest Mn^{3+}/Mn^{4+} atomic ratio (5.49), followed by OL-1 nanowires (3.90), while OL-1 nanosheets have the lowest Mn^{3+}/Mn^{4+} atomic ratio (0.72).

Table 1. Surface Area, AOS of Mn, and Atomic Ratio of the Nanostructured OL-1 Samples

	atomic ratio			oxygen vacancy density		surface area ($m^2\ g^{-1}$)	micropore area ($m^2\ g^{-1}$)
samples	K/Mn ICP	Mn^{3+}/Mn^{4+} (Mn 2p)	AOS (Mn)	calcd. by Mn 2p	calcd. by AOS	multipoint BET	t-plot method
nanoflowers	0.10	5.49	3.13	0.39	0.39	162.6	45.4
nanowires	0.25	3.90	3.24	0.29	0.26	98.0	21.2
nanosheets	0.33	0.72	3.48	0.08	0.10	19.0	3.4

dx.doi.org/10.1021/am5027743 | ACS Appl. Mater. Interfaces 2014, 6, 14981−14987

The average oxidation state (AOS) of Mn in the OL-1 samples was calculated by using the magnitude of Mn 3s multiplet splitting according to the following formula:[46,47]

$$\mathrm{AOS} = 8.95 - 1.13\Delta E_s(\mathrm{eV})$$

where ΔE_s represents the multiplet spitting, which is the energy difference between the main peak and its satellite. As can been seen from Figure 3B, the obtained ΔE_s of OL-1 nanflowers, nanowires, and nanosheets is 5.15, 5.06, and 4.84 eV, respectively. The calculated AOS increases in the sequence of OL-1 nanoflowers (3.13) < OL-1 nanowires (3.23) < OL-1 nanosheets (3.48).

As all the OL-1 samples have the same birnessite structure and there is no evidence of other manganese oxide (e.g., Mn_2O_3, Mn_3O_4, etc.) phase as shown in Figure 1, the presence of Mn^{3+} in the OL-1 samples arise from the intercalation of K^+ cations into the layered OL-1 and/or the formation of oxygen vacancies to maintain electrostatic balance:[3,4,48]

$$Mn^{4+}O^{2-}{}_2 + xK^+ \rightarrow K^+{}_xMn^{4+}{}_{1-x}Mn^{3+}{}_xO^{2-}{}_2 \quad (1)$$

$$-Mn^{4+}-O^{2-}-Mn^{4+}- \rightarrow -Mn^{3+}-\square-Mn^{3+}- + \frac{1}{2}O_2 \quad (2)$$

The overall reaction is described as follows:

$$Mn^{4+}O_2^{2-} + xK^+ \rightarrow K^+{}_xMn_y^{4+}Mn_{1-y}^{3+}O_{2-z}^{2-} + \frac{z}{2}O_2 \quad (3)$$

where $y = 1 - x - 2z$

Thus, we calculated the oxygen vacancy concentration of the OL-1 samples according to both the K/Mn atomic ratio by ICP and the Mn^{3+}/Mn^{4+} atomic ratio by Mn 2p XPS spectra analysis. As shown in Table 1, OL-1 nanoflowers show the highest oxygen vacancy concentration (0.39), followed by OL-1 nanowires (0.29) and OL-1 nanosheets (0.08). The oxygen vacancy concentration of the OL-1 samples was also calculated according to the K/Mn atomic ratio and AOS of Mn. In this case, the oxygen vacancy concentration of the OL-1 nanoflowers, OL-1 nanowires, and OL-1 nanosheets is 0.39, 0.26, and 0.10, respectively, which is in general agreement to the corresponding value calculated by using Mn 2p XPS spectra analysis. These XPS results, together with XRD analysis, reveal that the OL-1 nanoflowers can maintain its structural integrity of birnessite despite a large number of oxygen vacancies or Mn^{3+}, which are very important for catalytic oxidation or release/storage of oxygen.

The lower AOS of OL-1 nanoflowers (3.13) than that of OL-1 nanosheets (3.48) is most probably attributed to the lower preparation temperature (50 °C) for OL-1 nanoflowers because the reaction at higher temperature (240 °C) is favorable for improving crystallinity of OL-1 evidenced by its sharper XRD peaks of OL-1 nanosheets than OL-1 nanoflowers (see Figure 1a and c), thus decreasing defects (e.g., oxygen vacancies) in OL-1.

3.2. Catalytic Activity. The effect of morphology on the catalytic activity of the OL-1 samples is investigated by evaluating the catalytic oxidation of benzene. Figure 4A shows the benzene conversion over the nanostructured OL-1 catalysts as a function of reaction temperature under the condition of benzene concentration = 2000 mg m^{-3} and space velocity (SV) = 48000 mL $g^{-1}{}_{-catal}$ h^{-1}. The reaction temperatures of T_{50} and T_{90} (corresponding to the benzene conversion = 50% and 90%, respectively) for the catalysts is compared (Table 2). As shown in Figure 4 and Table 2, OL-1 nanaosheets exhibit the lowest catalytic activity. Its T_{50} is 466 °C, and its benzene conversion is only 56.5% even at a reaction temperature of 480 °C. OL-1 nanowires show higher catalytic activity, its T_{50} and T_{90} decreases to 294 and 397 °C, respectively. OL-1 nanoflowers exhibit the highest catalytic activity, its T_{50} and T_{90} decreases to 192 and 232 °C, respectively. Remarkably, as compared to OL-1 nanosheets, OL-1 nanoflowers show a tremendous decrease (ΔT_{50} = 274 °C, ΔT_{90} > 248 °C) in the reaction temperature of T_{50} and T_{90}. These results indicate that the morphology has significant effect on the catalytic activity of the nanostructured OL-1. For comparison, we tested the catalytic activity of a commercial supported noble metal catalyst (0.5% Pt/Al_2O_3, 320.4 m^2 g^{-1}). Both T_{50} (204 °C) and T_{90} (260 °C) of 0.5% Pt/Al_2O_3 are higher than the corresponding values of OL-1 nanoflowers. The effect of the space velocity on the catalytic activity of the OL-1 nanoflower catalyst was investigated under the condition of benzene concentration =2000 mg m^{-3} and the reaction temperature at 240 °C (Supporting Information Figure S6). After increasing SV from 24000 to 48000 mL $g^{-1}{}_{-catal}$ h^{-1}, benzene conversion slightly decreases from 96.9% to 93.4%. Further increasing SV to 72000 and 96000 mL $g^{-1}{}_{-catal}$ h^{-1} leads to a decrease of benzene conversion to 71.2% and 55.8%, respectively. We also evaluated the long-term catalytic stability of the OL-1 nanoflower catalyst by using the benzene oxidation

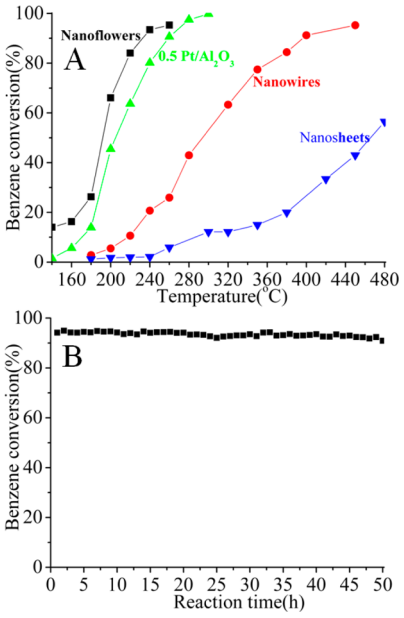

Figure 4. Benzene conversion versus reaction temperature (A) and reaction time over the OL-1 nanoflower catalyst for the benzene oxidation at 260 °C (B) under the condition of benzene concentration = 2000 mg m^{-3} and SV = 48000 mL g^{-1}_{-catal} h^{-1}.

Table 2. T_{50}, T_{90}, and Specific Rate of Benzene Oxidation over the Nanostructured OL-1 Catalysts

	catalytic activity (°C)		rate at 240 °C	specific rate at 240 °C
samples	T_{50}	T_{90}	μmol min^{-1}	μmol $m^{-2}_{-catalysts}$ min^{-1}
nanoflowers	192	232	0.958	0.118
nanowires	294	397	0.212	0.043
nanosheets	466		0.018	0.019

reaction test at 260 °C (Figure 4B). At the initial 4 h, the benzene conversion on OL-1 nanoflower catalyst is 94.1%. After 50 h, the benzene conversion remains 90.9%, suggesting that OL-1 nanoflowers exhibit good catalytic stability.

3.3. Origin of the Morphology-Dependent Catalytic Activity. The benzene reaction rates at 240 °C for the OL-1 catalysts are compared in Table 2. The benzene reaction rate of OL-1 nanoflowers (0.958 μmol min^{-1}) is 4.5 and 53.4 times higher than those of OL-1 nanowires and nanosheets, respectively. The question is why the nanostructured OL-1 catalysts with different morphologies exhibit quite different catalytic activity. It is well-known that the facet of nanostructured materials has effect on the catalytic activity due to the different surface energy.[49,50] However, the OL-1 catalysts has the same facet {100} in spite of their different morphology as shown in Figure 2 and Supporting Information Figure S3. To clarify whether the much higher catalytic activity of the OL-1 nanoflowers as compared to OL-1 nanowires and nanosheets mainly originates from their higher surface area (Table 1), their specific benzene reaction rates (per unit surface area of catalyst) at 240 °C, which represent the intrinsic catalytic efficiency of the OL-1 catalysts, are compared (Table 2). As shown in Table 2, OL-1 nanoflowers exhibit the highest specific benzene reaction rate (0.118 μmol m^{-2} min^{-1}), which is 2.7 and 6.2 times higher than those of OL-1 nanowires and nanosheets, respectively.

3.3.1. CO-TPR and O_2-TPO. It is commonly accepted that the catalytic oxidation on manganese oxide proceeds via the Mars–van Krevelen mechanism:[3,4,37,39] Organic molecules adsorbed on catalyst surface are oxidized by surface lattice oxygen, and the resultant oxygen vacancies are subsequently replenished by gas-phase O_2. Based on the mechanism, the fundamental and important thing for understanding and increasing the catalytic efficiency of OL-1 is to reveal the factors of affecting its lattice oxygen activity. As the OL-1 catalysts have the different concentration of Mn^{3+} or oxygen vacancy shown in the above XPS discussion (Table 1), the effect of Mn^{3+} or oxygen vacancy concentration on the lattice oxygen reactivity of the OL-1 samples was evaluated by CO-TPR. Figure 5A shows the CO-TPR profiles of the OL-1 samples. For OL-1 nanosheets with the lowest Mn^{3+} or oxygen vacancy concentration, the maximal CO consumption appears around 257 and 389 °C. These major peaks indicate a two-step reduction for MnO_2: MnO_2 to Mn_3O_4 and Mn_3O_4 to MnO.[25] Interestingly, compared to the corresponding TPR peaks of OL-1 nanosheets, increasing the Mn^{3+} or oxygen vacancy concentration in the OL-1 samples results in a considerable shift of the TPR peaks to lower temperature. When the Mn^{3+}/Mn^{4+} molar ratio increases from 0.72 to 3.90 (OL-1 nanowires), the lowest temperature peak (T_L) decreases from 257 to 219 °C while the highest temperature peak (T_H) remains almost unchanged. In addition, a lower temperature TPR peak around 330 °C is observed for OL-1 nanowires, suggesting the removal of three kinds of lattice oxygen in OL-1 nanowires by CO. Further increasing the Mn^{3+}/Mn^{4+} ratio to 5.49 (OL-1 nanoflowers) leads to a decrease of T_L and T_H to 185 and 363 °C, respectively. This result indicates that increasing Mn^{3+} or oxygen vacancy concentration in the OL-1 catalysts results in the significant improvement of the lattice oxygen activity, thus tremendously improving the catalytic activity for the benzene oxidation. The consumption amount of CO consumed for the OL-1 catalysts was quantitatively measured by calculating the area of their TPR profiles and

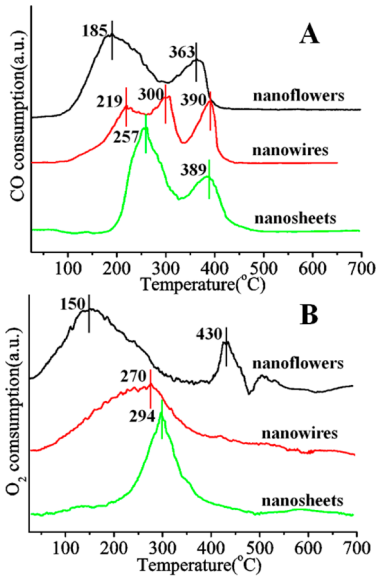

Figure 5. CO-TPR (A) and O_2-TPO (B) profiles of OL-1 samples with different morphologies.

the profile for a known amount of CO. The total consumption amount of CO for OL-1 nanoflowers, nanowires, and nanosheets is 7.36, 6.15, and 6.71 mmol g^{-1}, respectively. As the second step reduction of Mn_3O_4 to MnO takes place at the temperature higher than the reaction temperature for the catalytic oxidation of benzene, the lattice oxygen of OL-1 corresponding to the first step reduction of OL-1 to Mn_3O_4 is the catalytic active site. The consumption amount of CO corresponding to the first-step reduction of OL-1 to Mn_3O_4 for OL-1 nanoflowers, nanowires, and nanosheets, calculated by fitting their TPR profiles, are 5.01, 4.49, and 3.84 mmol g^{-1}, respectively. This result indicates that OL-1 nanoflowers have higher amount of active lattice oxygen than OL-1 nanowires and nanosheets, thus resulting in its higher catalytic activity (Figure 4 and Table 2).

O_2-TPO of the OL-1 samples prereduced at 220 °C for 1 h in the flow of 5 vol % CO/He was performed (Figure 5B). For the prereduced OL-1 nanoflowers, according to the assignment of the CO-TPR peaks as discussed above, the O_2 consumption occurs around 150 and 430 °C are assigned to two-step reoxidation for the OL −1 nanoflowers prereduced by CO: Mn_3O_4 to MnO_2 and MnO to Mn_3O_4, respectively. Compared to the prereduced OL-1 nanoflowers with the highest oxygen vacancy concentration, the prereduced OL-1 nanowires with lower Mn^{3+} or oxygen vacancy concentration exhibit the higher temperature reoxidation peak (270 °C). The prereduced OL-1 nanosheets with the lowest Mn^{3+} or oxygen vacancy concentration show the highest temperature reoxidation peak (294 °C). The consumption amount of O_2 for the prereduced OL-1 samples was quantitatively measured by calculating the area of their TPO profiles and the profile for a known amount of O_2. The total consumption amount of O_2 for the prereduced samples of OL-1 nanoflowers, OL-1 nanowires, and OL-1 nanosheets are 5.96, 4.36, and 3.84 mmol g^{-1}, respectively. The maximal reoxidation peak temperature of the OL-1 nanoflowers prereduced by CO is lower than the corresponding maximal reduction peak temperature of the OL-1 nanoflowers (Figure 5A). Although the maximal reoxidation peak temperature of OL-1 nanowires and nanosheets are higher than their corresponding maximal reduction peak temperature, their

start reoxidation temperature of ~50 and ~77 °C are lower than their corresponding start reduction temperature of ~100 and ~180 °C, respectively. These results reveal that reducibility or lattice oxygen activity of OL-1 plays a decisive role in its catalytic activity according to the Mars–van Krevelen mechanism.

3.3.2. DFT Calculation. To further confirm whether the enhancement of the lattice oxygen activity for OL-1 nanoflowers as compared to OL-1 nanowires and nanosheets originates from their higher oxygen vacancy concentration, the effect of the oxygen vacancy on the lattice oxygen activity of OL-1 is theoretically studied by calculating the energy of the removal of lattice oxygen (oxygen vacancy formation energy) using density functional theory (DFT) calculations. The oxygen vacancy formation energy in a calculated super cell (Figure 6) can be defined as[3,4]

$$E_{VO1} = E_{def1} - E_{bulk} + 0.5\,E_{O2} \quad (4)$$

$$E_{VO2} = E_{def2} - E_{def1} + 0.5\,E_{O2} \quad (5)$$

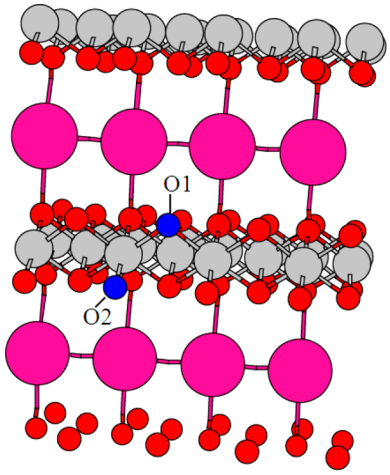

Figure 6. Calculated super cell of OL-1 ($K_8Mn_{32}O_{64}$): purple (K), gray (Mn), red (O), and blue (oxygen atom to be removed).

Here, E_{def1} is the system energy with loss of one oxygen atom (O1), E_{bulk} is the energy of a slab without loss of oxygen atom, E_{def2} is the system energy with loss of two oxygen atoms, and E_{O2} is the energy of an O_2 molecule in gas phase. The removal energy of the first lattice oxygen atom in the OL-1 super cell (E_{VO1}) is 3.51 eV. Interestingly, the removal energy of the second lattice oxygen atom adjacent to the oxygen vacancy (E_{VO2} = 3.37 eV) is lower than E_{VO1}. This result suggests that the presence of oxygen vacancy makes the lattice oxygen adjacent to the oxygen vacancy more active.

4. CONCLUSION

In summary, the OL-1 nanoflowers are prepared by hydrothermal redox reaction between $Mn(NO_3)_2$ and $KMnO_4$ at 50 °C. Their catalytic activity for benzene oxidation is compared with the catalysts of the OL-1 nanowires and nanosheets. The OL-1 nanoflowers exhibit tremendously higher catalytic activity for benzene oxidation than the OL-1 nanowires and nanosheets. The tremendous catalytic enhancement of the OL-1 nanoflowers compared to the OL-1 nanowires and nanosheets is attributed to their highest surface area as well as their highest lattice oxygen reactivity due to their higher concentration of oxygen vacancies or Mn^{3+}, thus tremendously improving the catalytic activity for the benzene oxidation. These results provide important insight for designing highly efficient catalysts of manganese oxide for both the partial oxidation and the complete oxidation of organic compounds in fine chemical production, environmental purification, fuel cells, etc.

■ ASSOCIATED CONTENT

Supporting Information

The thickness size distribution, SEM, TEM, N_2 adsorption–desorption isotherm, TG/DSC curves, and the effect of SV on the catalytic activity. This material is available free of charge via the Internet at http://pubs.acs.org.

■ AUTHOR INFORMATION

Corresponding Author

*Email: liyuanzhi66@hotmail.com.

Notes

The authors declare no competing financial interest.

■ ACKNOWLEDGMENTS

This work was supported by National Natural Science Foundation of China (21273169), Research and Development Project of Hubei Province (2013BAA045).

■ REFERENCES

(1) Huang, H. J.; Li, D. Z.; Lin, Q.; Zhang, W. J.; Shao, Y.; Chen, Y. B.; Sun, M.; Fu, X. Z. Efficient Degradation of Benzene over $LaVO_4$/TiO_2 Nanocrystalline Heterojunction Photocatalyst under Visible Light Irradiation. *Environ. Sci. Technol.* **2009**, *43*, 4164–4168.

(2) Mathur, A. K.; Majumder, C. B.; Chatterjee, S. Combined Removal of BTEX in Air Stream by Using Mixture of Sugar Cane Bagasse, Compost, and GAC as Biofilter Media. *J. Hazard. Mater.* **2007**, *148*, 64–74.

(3) Hou, J. T.; Li, Y. Z.; Liu, L. L.; Ren, L.; Zhao, X. J. Effect of Giant Oxygen Vacancy Defects on the Catalytic Oxidation of OMS-2 Nanorods. *J. Mater. Chem. A* **2013**, *1*, 6736–6741.

(4) Hou, J. T.; Liu, L. L.; Li, Y. Z.; Mao, M. Y.; Lv, H. Q.; Zhao, X. J. Tuning the K^+ Concentration in the Tunnel of OMS-2 Nanorods Significantly Improves Catalytic Activity for Benzene Oxidation. *Environ. Sci. Technol.* **2013**, *47*, 13730–13736.

(5) Liotta, L. F. Catalytic Oxidation of Volatile Organic Compounds on Supported Noble Metals. *Appl. Catal., B* **2010**, *100*, 403–412.

(6) Centeno, M. A.; Paulis, M.; Montes, M.; Odriozola, J. A. Catalytic Combustion of Volatile Organic Compounds on Au/CeO_2/Al_2O_3 and Au/Al_2O_3 Catalysts. *Appl. Catal., A* **2002**, *234*, 65–78.

(7) Fei, Z. Y.; Sun, B.; Zhao, L.; Ji, W. J.; Au, C. T. Strong Morphological Effect of Mn_3O_4 Nanocrystallites on the Catalytic Activity of Mn_3O_4 and Au/Mn_3O_4 in Benzene Combustion. *Chem.—Eur. J.* **2013**, *19*, 6480–6487.

(8) Kim, H. S.; Kim, T. W.; Koh, H. L.; Lee, S. H.; Min, B. R. Complete Benzene Oxidation over Pt-Pd Bimetal Catalyst Supported on γ-Alumina: Influence of Pt–Pd Ratio on the Catalytic Activity. *Appl. Catal., A* **2005**, *280*, 125–131.

(9) Liu, F.; Zuo, S.; Wang, C.; Li, J.; Xiao, F.; Qi, C. Pd/Transition Metal Oxides Functionalized ZSM-5 Single Crystals with *b*-axis Aligned Mesopores: Efficient and Long-lived Catalysts for Benzene Combustion. *Appl. Catal., B* **2014**, *148–149*, 106–113.

(10) Suib, S. L. Porous Manganese Oxide Octahedral Molecular Sieves and Octahedral Layered Materials. *Acc. Chem. Res.* **2008**, *41*, 479–487.

(11) Feng, Q.; Kanoh, H.; Ooi, K. Manganese Oxide Porous Crystals. *J. Mater. Chem.* **1999**, *9*, 319–333.

(12) Manning, B. A.; Fendorf, S. E.; Bostick, B.; Suarez, D. L. Arsenic(III) Oxidation and Arsenic(V) Adsorption Reactions on Synthetic Birnessite. *Environ. Sci. Technol.* **2002**, *36*, 976–981.

(13) Yin, H.; Liu, F.; Feng, X.; Liu, M.; Tan, W.; Qiu, G. Co^{2+}-Exchange Mechanism of Birnessite and Its Application for the Removal of Pb^{2+} and As(III). *J. Hazard. Mater.* **2011**, *196*, 318−326.
(14) Kim, S. H.; Kim, S. J.; Oh, S. M. Preparation of Layered MnO_2 via Thermal Decomposition of $KMnO_4$ and Its Electrochemical Characterizations. *Chem. Mater.* **1999**, *11*, 557−563.
(15) Aronson, B. J.; Kinser, A. K.; Passerini, S.; Smyrl, W. H.; Stein, A. Synthesis, Characterization, and Electrochemical Properties of Magnesium Birnessite and Zinc Chalcophanite Prepared by a Low-Temperature Route. *Chem. Mater.* **1999**, *11*, 949−957.
(16) Devaraj, S.; Munichandraiah, N. Effect of Crystallographic Structure of MnO_2 on Its Electrochemical Capacitance Properties. *J. Phys. Chem. C* **2008**, *112*, 4406−4417.
(17) Duan, X.; Yang, J.; Gao, H.; Ma, J.; Jiao, L.; Zheng, W. Controllable Hydrothermal Synthesis of Manganese Dioxide Nanostructures: Shape Evolution, Growth Mechanism, and Electrochemical Properties. *CrystEngComm* **2012**, *14*, 4196−4204.
(18) Zhu, H. T.; Luo, J.; Yang, H. X.; Liang, J. K.; Rao, G. H.; Li, J. B.; Du, Z. M. Birnessite-Type MnO_2 Nanowalls and Their-Magnetic Properties. *J. Phys. Chem. C* **2008**, *112*, 17089−17094.
(19) Ge, J.; Zhuo, L.; Yang, F.; Tang, B.; Wu, L.; Tung, C. One-Dimensional Hierarchical Layered K_xMnO_2 (x < 0.3) Nanoarchitectures: Synthesis, Characterization, and Their Magnetic Properties. *J. Phys. Chem. B* **2006**, *110*, 17854−17859.
(20) Hocking, R. K.; Brimblecombe, R.; Chang, L. Y.; Singh, A.; Cheah, M. H.; Glover, C.; Casey, W. H.; Spiccia, L. Water-Oxidation Catalysis by Manganese in a Geochemical-like Cycle. *Nat. Chem.* **2011**, *3*, 461−466.
(21) Iyer, A.; Del-Pilar, J.; King'ondu, C. K.; Kissel, E.; Garces, H. F.; Huang, H.; El-Sawy, A. M.; Dutta, P. K.; Suib, S. L. Water Oxidation Catalysis Using Amorphous Manganese Oxides, Octahedral Molecular Sieves(OMS-2), and Octahedral Layered (OL-1) Manganese Oxide Structures. *J. Phys. Chem. C* **2012**, *116*, 6474−6483.
(22) Xiao, W.; Wang, D.; Lou, X. W. Shape-Controlled Synthesis of MnO_2 Nanostructures with Enhanced Electrocatalytic Activity for Oxygen Reduction. *J. Phys. Chem. C* **2009**, *114*, 1694−1700.
(23) Chen, H.; He, J.; Zhang, C.; He, H. Self-Assembly of Novel Mesoporous Manganese Oxide Nanostructures and Their Application in Oxidative Decomposition of Formaldehyde. *J. Phys. Chem. C* **2007**, *111*, 18033−18038.
(24) Tian, H.; He, J.; Liu, L.; Wang, D.; Hao, Z.; Ma, C. Highly Active Manganese Oxide Catalysts for Low-Temperature Oxidation of Formaldehyde. *Microporous Mesoporous Mater.* **2012**, *151*, 397−402.
(25) Zhou, L.; Zhang, J.; He, J.; Hu, Y.; Tian, H. Facile In-Situ Synthesis of Manganese Dioxide Nanosheets on Cellulose Fibers and Their Application in Oxidative Decomposition of Formaldehyde. *Mater. Res. Bull.* **2011**, *46*, 1714−1722.
(26) Parida, K. M.; Samal, A. Catalytic Combustion of Volatile Organic Compounds on Indian Ocean Manganese Nodules. *Appl. Catal., A* **1999**, *182*, 249−256.
(27) Zhou, L.; He, J.; Zhang, J.; He, Z.; Hu, Y.; Zhang, C.; He, H. Facile In-Situ Synthesis of Manganese Dioxide Nanosheets on Cellulose Fibers and Their Application in Oxidative Decomposition of Formaldehyde. *J. Phys. Chem. C* **2011**, *115*, 16873−16878.
(28) Liang, S.; Teng, F.; Bulgan, G.; Zong, R.; Zhu, Y. Effect of Phase Structure of MnO_2 Nanorod Catalyst on the Activity for CO Oxidation. *J. Phys. Chem. C* **2008**, *112*, 5307−5315.
(29) Atribak, I.; Bueno-Loipez, A.; Garcia-Garcia, A.; Navarro, P.; Frias, D.; Montes, M. Catalytic Activity for Soot Combustion of Birnessite and Cryptomelane. *Appl. Catal., B* **2010**, *93*, 267−273.
(30) Nakayama, M.; Shamoto, M.; Kamimura, A. Surfactant-Induced Electrodeposition of Layered Manganese Oxide with Large Interlayer Space for Catalytic Oxidation of Phenol. *Chem. Mater.* **2010**, *22*, 5887−5894.
(31) Kamimura, A.; Nozaki, Y.; Nishiyama, M.; Nakayama, M. Oxidation of Benzyl Alcohols by Semi-Stoichiometric Amounts of Cobalt-Doped Birnessite-Type Layered MnO_2 under Oxygen Atmosphere. *RSC Adv.* **2013**, *3*, 468−472.
(32) Kresse, G.; Hafner, J. Ab Initio Molecular Dynamics for Liquid Metals. *Phys. Rev. B* **1993**, *47*, 558−561.
(33) Kresse, G.; Hafner, J. Ab Initio Molecular-Dynamics Simulation of the Liquid−Metal−Amorphous-Semiconductor Transition in Germanium. *Phys. Rev. B* **1994**, *49*, 14251−14269.
(34) Kresse, G.; Furthmuller, J. Efficiency of Ab-Initio Total Energy Calculations for Metals and Semiconductors Using a Plane-Wave Basis Set. *Comput. Mater. Sci.* **1996**, *6*, 15−50.
(35) Blochl, P. E. Projector Augmented-Wave Method. *Phys. Rev. B* **1994**, *50*, 17953−17979.
(36) Kresse, G.; Joubert, D. From Ultrasoft Pseudopotentials to the Projector Augmented-Wave Method. *Phys. Rev. B* **1999**, *59*, 1758−1775.
(37) Kresse, G.; Hafner, J. Ab Initio Molecular Dynamics for Open-Shell Transition Metals. *Phys. Rev. B* **1993**, *48*, 13115−13118.
(38) Kwon, K. D.; Refson, K.; Sposito, G. Defect-Induced Photoconductivity in Layered Manganese Oxides: A Density Functional Theory Study. *Phys. Rev. Lett.* **2008**, *100*, 146601.
(39) Leofanti, G.; Padovanb, M.; Tozzolac, G.; Venturelli, B. Surface Area and Pore Texture of Catalysts. *Catal. Today* **1998**, *41*, 207−219.
(40) Ahmeda, K. A. M.; Huang, K. Synthesis, Characterization, and Catalytic Activity of Birnessite Type Potassium Manganese Oxide Nanotubes and Nanorods. *Chem. Phys. Mater.* **2012**, *133*, 605−610.
(41) Santos, V. P.; Pereira, M. F. R.; Orfao, J. J. M.; Figueiredo, J. L. The Role of Lattice Oxygen on the Activity of Manganese Oxides Towards the Oxidation of Volatile Organic Compounds. *Appl. Catal., B* **2010**, *99*, 353−363.
(42) Wei, Y. J.; Yan, L. Y.; Wang, C. Z.; Xu, X. G.; Wu, F.; Chen, G. Effects of Ni Doping on $[MnO_6]$ Octahedron in $LiMn_2O_4$. *J. Phys. Chem. B* **2004**, *108*, 18547−18551.
(43) Tan, B. J.; Klabunde, K. J.; Sherwood, P. M. A. XPS Studies of Solvated Metal Atom Dispersed (SMAD) Catalysts. Evidence for Layered Cobalt-Manganese Particles on Alumina and Silica. *J. Am. Chem. Soc.* **1991**, *113*, 855−861.
(44) Genuino, H. C.; Dharmarathna, S.; Njagi, E. C.; Mei, M. C.; Suib, S. L. Gas-Phase Total Oxidation of Benzene, Toluene, Ethylbenzene, and Xylenes Using Shape-Selective Manganese Oxide and Copper Manganese Oxide Catalysts. *J. Phys. Chem. C* **2012**, *116*, 12066−12078.
(45) Wang, F.; Dai, H. X.; Deng, J. G.; Bai, G. M.; Ji, K. M.; Liu, Y. X. Manganese Oxides with Rod-, Wire-, Tube-, and Flower-Like Morphologies: Highly Effective Catalysts for the Removal of Toluene. *Environ. Sci. Technol.* **2012**, *46*, 4034−4041.
(46) Santos, V. P.; Soares, O. S. G. P.; Bakker, J. J. W.; Pereira, M. F. R.; Orfao, J. J. M.; Gascon, J.; Kapteijn, F.; Figueiredo, J. L. Structural and Chemical Disorder of Cryptomelane Promoted by Alkali Doping: Influence on Catalytic Properties. *J. Catal.* **2012**, *293*, 165−174.
(47) Sun, M.; Lan, B.; Lin, T.; Cheng, G.; Ye, F.; Yu, L.; Cheng, X.; Zheng, X. Controlled Synthesis of Nanostructured Manganese Oxide: Crystalline Evolution and Catalytic Activities. *CrystEngComm* **2013**, *15*, 7010−7018.
(48) Feng, Q.; Kanoh, H.; Miyai, Y.; Ooi, K. Alkali Metal Ions Insertion/Extraction Reactions with Hollandite-Type Manganese Oxide in the Aqueous Phase. *Chem. Mater.* **1995**, *7*, 148−153.
(49) Wu, Z. L.; Li, M. J.; Overbury, S. H. On the Structure Dependence of CO Oxidation over CeO_2 Nanocrystals with Well-Defined Surface Planes. *J. Catal.* **2012**, *285*, 61−73.
(50) Shi, W. Q.; Li, Y. Z.; Hou, J. T.; Lv, H. Q.; Zhao, X. J.; Fang, P. F.; Zheng, F.; Wang, S. J. Densely Populated Mesopores in Microcuboid CeO_2 Crystal Leading to a Significant Enhancement of Catalytic Activity. *J. Mater. Chem. A* **2013**, *1*, 728−734.